Wide-Band Steady-State Numerical Model and Parameter Extraction of a Tensile-Strained Bulk Semiconductor Optical Amplifier

Michael J. Connelly, *Member, IEEE*

Abstract—**A wide-band steady-state model of a tensile-strained bulk InGaAsP semiconductor optical amplifier is described. An efficient numerical algorithm of the steady-state model and a parameter extraction algorithm based on the Levenberg–Marquardt method are described. The parameter extraction technique is used to determine the material Auger recombination coefficient, effective intraband lifetime, the average strain and molar fraction of Arsenic in the active region. Simulations and comparisons with experiment are given which demonstrate the accuracy and versatility of the model.**

Index Terms—**Modeling, parameter extraction, semiconductor optical amplifier, tensile-strained bulk material.**

I. INTRODUCTION

SEMICONDUCTOR optical amplifier (SOA) technology has matured to the point where commercial devices are available for use in optical communication systems [1]. Mathematical models are required to aid in the design of SOAs and to predict their operational characteristics. Previously we have developed a wide-band steady-state numerical model of an unstrained bulk SOA [2], [3]. Such SOAs have low-polarization sensitivity; however, the necessity for a square cross section active waveguide makes fabrication difficult. Polarization insensitive SOAs can be fabricated using tensile-strained bulk material and a conventional rectangular cross section waveguide. The introduction of the appropriate amount of tensile strain can be used to compensate for the different confinement factors experienced by the waveguide transverse electric (TE) and transverse magnetic (TM) modes. In this paper we extend the model developed in [2], [3] to a comprehensive wide-band steady-state model of a tensile-strained bulk InGaAsP SOA. A new parameter extraction algorithm based on the Levenberg–Marquardt method and measurements of SOA spontaneous emission spectrum is used to estimate model parameters such as the Auger recombination coefficient and effective intraband lifetime.

II. AMPLIFIER STRUCTURE AND MATERIAL GAIN MODEL

A. SOA Geometry and Material

The SOA is manufactured by Kamelian and has an undoped $In_{1-x}Ga_xAs_yP_{1-y}$ active region between two InGaAsP sepa-
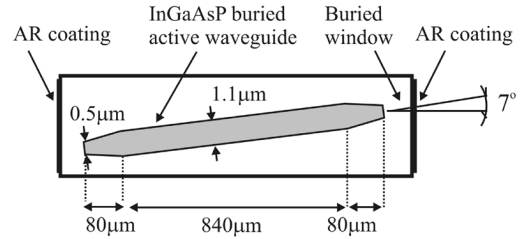
Fig. 1. Tensile-strained bulk SOA—top view of the active waveguide.

rate-confinement heterostructure (SCH) layers and operates in the 1.55-μm region. A top view of the active waveguide is shown in Fig. 1. y and x are the molar fractions of arsenide and gallium in the active region. The device structure consists of central active region waveguide of width W_c, thickness d, and length L_c. The active region narrows linearly as a lateral taper of length L_t to width W_t at each end. Pertinent geometrical and material parameters for the device under consideration are given in Table I. Because of the waveguide asymmetry, the optical confinement factors of the TE and TM modes are not equal. In addition, because of the tapers, the confinement factors are a function of the active waveguide width. The central region TE and TM confinement factors are 0.18 and 0.12, respectively. The confinement factors are modeled by [4]

$$\Gamma_{TE}(z) = 0.189 \frac{[5.66 W(z)]^2}{2 + [5.66 W(z)]^2}$$

$$\Gamma_{TM}(z) = 0.126 \frac{[5.66 W(z)]^2}{2 + [5.66 W(z)]^2} \tag{1}$$

where the waveguide width W is given in microns. It is assumed that the ratio of the TE and TM confinement factors is constant, although for small waveguide widths this assumption is no longer valid [5]. z is the distance from the SOA input facet. The nominal biaxial tensile strain is 0.2%, although the actual value of strain can be less than the design strain due to relaxation effects, which become larger as the active region thickness decreases [6]. For this small value of strain, we take x to be equal to that obtained using the lattice matching expression for matching to InP [7]

$$x = \frac{0.1894y}{0.4184 - 0.013y}. \tag{2}$$

The active region bandgap energy, with no injected carriers, is given by [6]

$$E_{g0} = 1.35 - 0.775y + 0.149y^2 \text{ eV.} \tag{3}$$

TABLE I
TENSILE-STRAINED BULK SOA GEOMETRICAL AND MATERIAL PARAMETERS

Symbol	Parameter	Value
L_c	Central active region length	840 μm
L_t	Taper length	80 μm
d	Active region thickness	0.1 μm
W_c	Central active region width	1.1 μm
W_t	Final taper width	0.5 μm
η_{in}	Input coupling loss	2 dB
η_{out}	Output coupling loss	2 dB
α_0	Intrinsic material absorption	3000 m^{-1}
α_1	Free electron loss coefficient	2.58 x 10^{-21} m^2 [11]
α_2	Intervalence band absorption coefficients	4.252 x 10^{-20} m^2 [11]
α_e		3.657 eV^{-1} [11]
K_g	Bandgap shrinkage coefficient	3.2 x 10^{-10} eVm^{-1} [7]
n_r	Active region refractive index	3.56
m_c	CB effective mass	(0.08 - 0.039y)m$_0$ [6]
b_{GaAs}, b_{InAs}, b_{InP}, b_{GaP}	Axial deformation potentials – GaAs, InAs, InP, GaP	-1.7, -1.8, -1.7, -1.8, eV [6]
Δ_{GaAs}, Δ_{InAs}, Δ_{InP}, Δ_{GaP}	Spin split off energies – GaAs, InAs, InP, GaP	0.34, 0.38, 0.11, 0.08 eV [6]
$E_{p,GaAs}$, $E_{p,InAs}$, $E_{p,InP}$, $E_{p,GaP}$	Optical matrix parameters – GaAs, InAs, InP, GaP	25.7, 22.2, 20.7, 22.2 eV [6]
$\gamma_{1,2,3,GaAs}$	Luttinger coefficients – GaAs ($\hbar^2/2m_0$)	6.98, 2.06, 2.93 [6]
$\gamma_{1,2,3,InAs}$	Luttinger coefficients – InAs ($\hbar^2/2m_0$)	20.0, 8.5, 9.2 [6]
$\gamma_{1,2,3,InP}$	Luttinger coefficients – InP ($\hbar^2/2m_0$)	5.08, 1.6, 2.1 [6]
$\gamma_{1,2,3,GaP}$	Luttinger coefficients – GaP ($\hbar^2/2m_0$)	4.05, 0.49, 2.93 [6]

If bandgap shrinkage is taken into account then the actual bandgap energy E_g is related to the carrier density n by [8]

$$E_g = E_{g0} - K_g n^{1/3} \qquad (4)$$

where K_g is the bandgap shrinkage coefficient. In this paper we take K_g to be equal to that for GaAs. The active region axial deformation potential b, spin orbit split off energy Δ, optical matrix parameter E_p, and Luttinger coefficients γ_1, γ_2, and γ_3 are obtained using the general interpolation expression

$$\begin{aligned} X = &X_{InP}(1-x)(1-y) \\ &+ X_{InAs}(1-x)y + X_{GaP}x(1-y) + X_{GaAs}xy \end{aligned} \qquad (5)$$

where X is the parameter of interest.

B. Band Structure

The active region consists of a thin epilayer (InGaAsP) of lattice constant a_e sandwiched between InGaAsP SCH layers of lattice constant a_s(equal to that for InP). The strain in the layer plane is

$$\varepsilon = \frac{(a_s - a_e)}{a_e}. \qquad (6)$$

For a small axial strain, as is the case in this paper, the heavy hole and light hole bands are each shifted by energy S, with respect to the mean valence band (VB) energy, given by

$$S = -b\varepsilon_{ax} \qquad (7)$$

where ε_{ax} is the axial strain. In the case of tetrahedral semiconductors we have $\varepsilon_{ax} \approx -2\varepsilon$ so we can rewrite (7) as

$$S = 2b\varepsilon. \qquad (8)$$

VB structure calculations on strained bulk material require a 6×6 Hamiltonian in an X, Y, Z basis, which includes the split-off band. In [9], the 6×6 Hamiltonian is simplified by using an axial approximation and choosing new basis states given by

$$|X\alpha\rangle = \frac{1}{\sqrt{2}}(|X \uparrow\rangle + i|X \downarrow\rangle)$$

$$|X\beta\rangle = \frac{1}{\sqrt{2}}(|X \uparrow\rangle + i|X \downarrow\rangle)$$

$$|Y\alpha\rangle = \frac{1}{\sqrt{2}}(|Y \uparrow\rangle - i|Y \downarrow\rangle)$$

$$|Y\beta\rangle = \frac{1}{\sqrt{2}}(|Y \uparrow\rangle - i|Y \downarrow\rangle)$$

$$|Z\alpha\rangle = \frac{1}{\sqrt{2}}(|Z \uparrow\rangle + i|Z \downarrow\rangle)$$

$$|Z\beta\rangle = \frac{1}{\sqrt{2}}(|Z \uparrow\rangle + i|Z \downarrow\rangle). \qquad (9)$$

The 3×3 Hamiltonian for the α states has the form

$$H = \begin{bmatrix} \alpha + A - B & -iA & C + i\Delta \\ i\Delta & \alpha + A + B & \Delta \\ C - i\Delta & \Delta & \alpha - 2A \end{bmatrix} \qquad (10)$$

where

$$\alpha = -\frac{\gamma_1 k^2}{2} - \Delta \quad B = \frac{3}{2}\bar{\gamma}k_t^2 \quad A = \gamma_2\left(k_z^2 - \frac{k_t^2}{2}\right) + S$$

$$C = -3\gamma_3 k_t k_z \quad \bar{\gamma} = \left[\left(\gamma_2^2 + \gamma_3^2\right)/2\right]^{1/2} \quad k^2 = k_t^2 + k_z^2.$$

$$(11)$$

The transverse and longitudinal components of the momentum vector are given by

$$k_t = k\sin\theta; \quad k_Z = k\cos\theta \qquad (12)$$

where k is the magnitude of the momentum vector and θ its azimuth. In the axial approximation the polar angle $\phi = 0$. $\mathbf{H}$ can be used to determine the VB structure and matrix elements required for the material gain calculations in Section–II.D. In the case of tensile strain the largest, intermediate and smallest eigenvalues of $\mathbf{H}$ correspond to the doubly degenerate light-hole (LH), heavy-hole (HH), and split-off (SO) bands, respectively. The conduction band (CB) energy-momentum relationship is given by [9]

$$E_c(k) = \frac{\hbar^2}{m_0}k^2 + \frac{P^2 m_c}{\hbar^2}\left\{\left[\frac{(\hbar^2 k)^2}{P^2 m_c^2} + 1\right]^2 - 1\right\} \qquad (13)$$

where m_0 is the electron mass, m_c is the CB effective electron mass, $P^2 = \hbar^2 M_0^2/m_0^2$ and the momentum matrix element is $M_0^2 = E_p m_0 e/2$.

C. Quasi-Fermi Levels

The active region quasi-Fermi levels can be obtained from the equation of charge neutrality. In the case of the CB the charge neutrality equation is

$$n = \int_0^\infty \frac{k^2}{\pi^2} f_c(E_c(k))\,dk. \qquad (14)$$

In the case of the VB the charge neutrality equation is given by

$$n = \sum_{b=\text{HH,LH}} \int_0^\infty dk \int_0^\pi \frac{k^2\sin\theta}{2\pi^2} f_v(E_{v,b}(k,\theta))\,d\theta \qquad (15)$$

where $E_{v,b}$ is the valence band energy and it is assumed that the number of holes in the VB equals the carrier density. In (15), the summation extends over the LH, HH bands. The SO band has a negligible effect on the Fermi-level. The Fermi–Dirac distributions in the CB and VB are given by

$$f_c(E_c) = \left[1 + \exp\left(\frac{E_c - E_{\text{fc}}}{kT}\right)\right]^{-1}$$

$$f_v(E_{v,b}) = \left[1 + \exp\left(\frac{E_{\text{fv}} - E_{v,b}}{kT}\right)\right]^{-1} \qquad (16)$$

where E_{fc} and E_{fv} are the CB and VB quasi-Fermi levels, respectively. For a given n, (14) and (15) can be solved numerically to determine E_{fc} and E_{fv}. Plots of the quasi-Fermi levels as a function of carrier density, using the value of y obtained in Section VI are shown in Fig. 2.
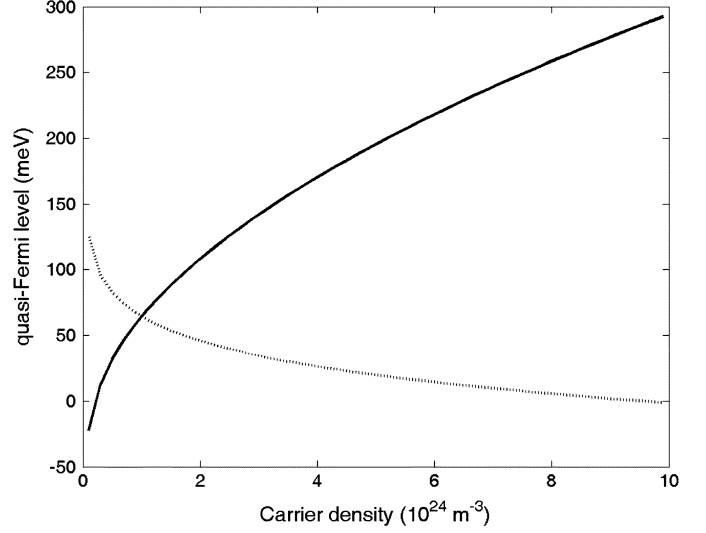

Fig. 2. Quasi-Fermi levels with respect to the unstrained band edge in the conduction band (solid line) and valence bands (dotted line) versus carrier density.

D. Material Gain

The TM and TE material gain coefficients at photon energy $\hbar\omega$ are given by [9]

$$g_{m,\text{TM}}(\hbar\omega)$$
$$= \frac{C_g}{\hbar\omega} \sum_{b=\text{LH,HH,SO}} \int_0^\infty \int_0^\pi k^2\sin\theta |M_{\text{TM},b}(k,\theta)|^2 L_z$$
$$\times L(E_{\text{cv},b}(k,\theta))[f_c(k) + f_{v,b}(k,\theta) - 1]\,d\theta\,dk$$

$$g_{m,\text{TE}}(\hbar\omega)$$
$$= \frac{C_g}{\hbar\omega} \sum_{b=\text{LH,HH,SO}} \int_0^\infty \int_0^\pi k^2\sin\theta |M_{\text{TE},b}(k,\theta)|^2 L_z$$
$$\times L(E_{\text{cv},b}(k,\theta))[f_c(k) + f_{v,b}(k,\theta) - 1]\,d\theta\,dk \qquad (17)$$

where

$$C_g = \frac{e^2\hbar}{2\pi\varepsilon_0 cm_0^2 n_r} \qquad (18)$$

where ε_0 is the permittivity of free space, c the speed of light in free-space and n_r the material refractive index. The CB to VB transition energies are given by

$$E_{\text{cv},b}(k,\theta) = E_c(k) - E_{v,b}(k,\theta) + E_g. \qquad (19)$$

The TM matrix element is given by

$$|M_{\text{TM},b}|^2 = \left|\alpha_z^b(k,\theta)\right|^2 |M_0|^2 \qquad (20)$$

where $\alpha_z^b(k,\theta)$ is the $|Z\rangle$ component of the corresponding b (LH, HH, or SO) eigenvector of $\mathbf{H}$. The TE matrix element is given by

$$|M_{\text{TM},b}|^2 = \frac{1}{2}\left(1 - \left|\alpha_z^b(k,\theta)\right|^2\right)|M_0|^2. \qquad (21)$$

Intraband relaxation and possible doping effects lead to a broadening of the gain spectrum. This effect is taken into account
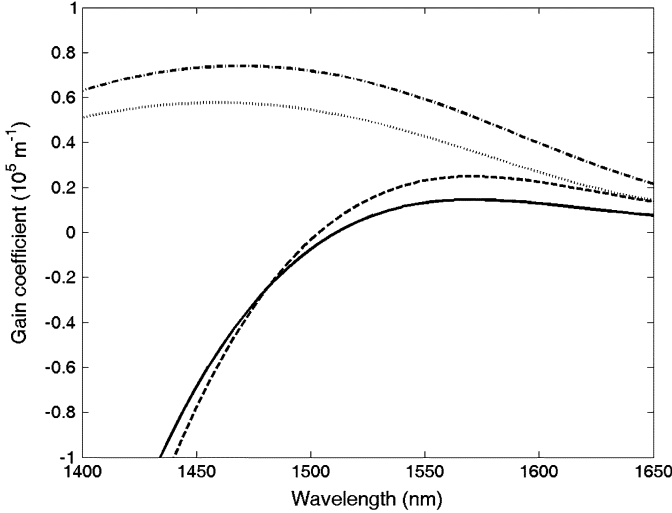
Fig. 3. Typical active region material gain (TM: solid line; TE: dashed line) and spontaneous emission gain coefficients (TM: dash-dot line; TE: dotted line). The carrier density is 3×10^{24} m^{-3}.
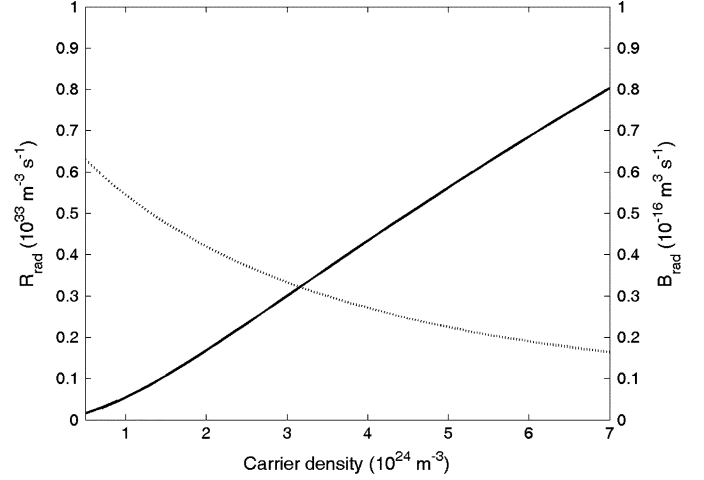

Fig. 4. Typical plots of the radiative recombination rate (solid line) and the bimolecular recombination coefficient (dotted line) versus carrier density.

using a sech line broadening function, which is a more accurate approximation to the real lineshape than the conventional Lorentzian lineshape function, [10]

$$L(E_{cv}) = \frac{\tau_r}{\hbar\pi} \operatorname{sech} \left[\frac{\tau_r}{\hbar}(E_{cv} - \hbar\omega) \right] \qquad (22)$$

where τ_r is the effective intraband relaxation time. In an undoped material τ_r is solely due to intraband relaxation and has a typical value of 0.1 ps [10]. However, when the material is highly doped, the resulting band tails dominate and τ_r can be much less than 0.1 ps.

The spontaneous emission gain coefficients $g_{sp,TM}$ and $g_{sp,TE}$ can be obtained by replacing the factor $f_c + f_{v,b} - 1$ in (17) by $f_c f_{v,b}$. Typical plots of the material gain and spontaneous emission gain versus wavelength, obtained using the parameters extracted in Section VI are shown in Fig. 3. The radiative recombination rate is given by [9]

$$R_{rad} = C_r \sum_{b=\text{LH,HH,SO}} \int_0^\infty \int_0^\infty \int_0^\pi (\hbar\omega)k^2 \sin\theta f_c(k)$$
$$\times [1 - f_{v,b}(k,\theta)]L(E_{cv,b}(k,\theta)) \, d\theta \, dk \, d(\hbar\omega) \quad (23)$$

where

$$C_r = \frac{e^2 n_r M_0^2}{6\pi^3 \varepsilon_0 m_0^2 \hbar^2 c^3}. \qquad (24)$$

A convenient analytical approximation for (23) is

$$R_{rad} = B_{rad}n^2 \approx (B_0 - B_1 n - B_2 n^2 - B_3 n^3)n^2 \quad (25)$$

where B_{rad} is the bimolecular recombination coefficient. Plots of R_{rad} and B_{rad} $(=R_{rad}/n^2)$ versus carrier density using the parameters extracted in Section VI and numerical integration of (23) are shown in Fig. 4. As shown in Fig. 4 R_{rad} is approximately a linear function of carrier density. In SOA models B_{rad} is often expressed as a polynomial function of n. In this case a cubic polynomial fit with coefficients B_0, B_1, B_2 and B_3 given by 0.74×10^{-16} m^{3}s^{-1}, 2.08×10^{-41} m^{6}s^{-1}, -2.96×10^{-66}

m^{9}s^{-1} and 1.67×10^{-91} m^{12}s^{-1} is a good fit to the calculated B_{rad}.

III. TRAVELING-WAVE MODEL

The model is based on a set of coupled differential equations that describe the interaction between the internal variables of the amplifier, i.e., the carrier density and the signal and amplified spontaneous emission (ASE) photon rates. It is assumed that transverse variations in the carrier density and photon rates are negligible. The traveling-wave equations for the complex amplitude $E_{s,p}^\pm$ of an amplified signal of polarization p (TE or TM) are given by [2]

$$\frac{dE_{s,p}^\pm(z)}{dz} = \left[\pm\frac{1}{2}g_p(\hbar\omega_s) \mp j\beta_p(n(z)) \right] E_{s,p}^\pm(z) \qquad (26)$$

where $+$ and $-$ denote traveling-waves in the positive and negative z directions, respectively The modulus squared of the amplitude of a traveling-wave is taken to be equal to its photon rate (s^{-1}). The polarization dependent propagation constant is given by

$$\beta_p = \frac{\hbar\omega_s \, n_{\text{eff},p}}{\hbar c} \qquad (27)$$

where $\hbar\omega_s$ is the signal photon energy and $n_{\text{eff},p}$ is the effective index of the waveguide for polarization p, which can be determined from the ripples in the ASE polarization resolved spectra. Equation (26) is subject to the boundary conditions

$$E_{s,p}^+(0) = (1 - \sqrt{R_1})E_{in,p} + \sqrt{R_1}E_{s,p}^-(0)$$
$$E_{s,p}^-(L) = \sqrt{R_2}E_{s,p}^+(L) \qquad (28)$$

where R_1 and R_2 are the facet reflectivities and the input signal amplitude is given by

$$E_{in,p} = \sqrt{\frac{\eta_{in}P_{in,p}}{\hbar\omega_s}} \qquad (29)$$

where $P_{in,p}$ is the input signal power (with polarization p) and η_{in} the input coupling loss. While the amplification of a coherent input signal must be described in terms of waves with definite

amplitude and phase, it is sufficient to describe the propagation of the ASE in terms of power only. To model the amplified spontaneous emission, we use a spectral slicing scheme whereby the ASE is split into a number of slices with photon energy

$$\hbar\omega_k = E_0 + kdE, \quad k = 1\ldots N_s \quad (30)$$

where E_0 is the starting energy, dE the spectrum slice energy width, and N_s the number of slices. If the facet reflectivities are nonzero then these energies are assumed to be equal to an integer multiple of the SOA cavity resonance longitudinal model frequency spacing. The traveling-wave equations for the spontaneous emission rates are given by [2]

$$\frac{dN_{p,k}^\pm}{dz} = \pm g_p(\hbar\omega_k, n)N_{p,k}^\pm \pm R_{\text{sp},p}(\hbar\omega_k, n) \quad (31)$$

where $N_{p,k}^+$ is the kth ASE photon rate spectral slice with polarization p (TE or TM) traveling in the positive z-direction. $N_{p,k}^-$ is the kth ASE photon rate spectral slice of polarization p (TE or TM) traveling in the negative z-direction. Equation (31) is subject to the boundary conditions

$$N_{p,k}^+(z = 0) = R_1 N_{p,k}^-(z = 0)$$
$$N_{p,k}^-(z = L) = R_2 N_{p,k}^+(z = L). \quad (32)$$

$R_{\text{sp},p}$ is the spontaneously emitted noise coupled into $N_{p,k}^+$ or $N_{p,k}^-$ and is given by [2]

$$R_{\text{sp},p}(\hbar\omega_k, n) = \Gamma_p(z)g_{\text{sp},p}(\hbar\omega_k, n)\,dE/h \quad (33)$$

The net gain coefficient at energy $\hbar\omega$ is given by

$$g_p(\hbar\omega, n) = \Gamma_p g_{m,p} - \alpha_p(\hbar\omega, n). \quad (34)$$

The polarization dependent optical loss coefficient, which is a function of energy and carrier density, is modeled as

$$\alpha_p(\hbar\omega, n) = \alpha_0 + \Gamma_p[\alpha_1 + \alpha_2\exp(-\alpha_e\hbar\omega)]n \quad (35)$$

where α_0 is the intrinsic material absorption and α_1 the free electron loss coefficient. α_2 and α_e are coefficients modeling intervalence band absorption [11].

IV. CARRIER DENSITY RATE EQUATION

The carrier density at z is determined from the rate equation

$$\frac{dn}{dt} = \frac{\eta(z)I}{ed[W_c(L_t + L_c) + W_t L_t]}$$
$$- R(n) - \frac{\Gamma_{s,p}}{dW(z)}g_{m,p}(\hbar\omega_s, n)$$
$$\times [|E_{s,p}^+(z)|^2 + |E_{s,p}^-(z)|^2]$$
$$- \frac{1}{dW(z)}\sum_{p=\text{TE,TM}}\sum_{k=0}^{N_s}\Gamma_p(z)g_{m,p}(\hbar\omega_k, n)K_{p,k}$$
$$\times [N_{p,k}^+(z) + N_{p,k}^-(z)] \quad (36)$$

where I is the bias current. The total quantum efficiency $\eta(z) = \eta_{\text{tr}}\eta_{\text{block}}(z)$, where η_{tr} is the (transport) efficiency that the injected carriers reach the active region. This is assumed to

be equal to unity in this paper. The pump blocking efficiency $\eta_{\text{block}}(z)$ is given by [12]

$$\eta_{\text{block}}(z) = \left[\frac{\int_0^\infty \frac{k^2 f_{c,0}(E_c)}{1 - f_c(E_c)}\,dk}{\int_0^\infty k^2 f_{c,0}(E_c)\,dk}\right]. \quad (37)$$

This is due to the fact that the presence of carriers in the active region reduces the efficiency of the pumping since only one carrier can occupy each quantum state. $f_{c,0}(E_c)$ is the Fermi–Dirac distribution for carriers in the CB when no stimulated emission terms are is present in (36). The quasi-Fermi level in this case is obtained by solving for the carrier density n_0 using the reduced form of (36)

$$\frac{\eta_{\text{tr}}I}{ed[W_c(L_t + L_c) + W_t L_t]} - R(n_0) = 0 \quad (38)$$

and obtaining the resulting quasi-Fermi level from (14). Equation (38) can be solved using the numerical bisection method.

The carrier recombination rate is given by

$$R(n) = A_{\text{tr}}n + R_{\text{rad}}(n) + C_{\text{aug}}n^3 \quad (39)$$

which includes the nonradiative processes of trap recombination (A_{tr}), which is taken to be proportional to n, and Auger recombination (C_{aug}), which is usually taken to be proportional to n^3. It is assumed that $A_{\text{tr}} = 0$ (i.e., the level of material defects is low). The principle nonradiative recombination mechanism in SOAs is usually Auger recombination due to the high carrier densities usually encountered. The normalization factor $K_{p,k}$, which accounts for the noise filtering introduced by the SOA resonances, is given by [13]

$$K_{p,k} = \frac{1}{\sqrt{1 + \gamma_{p,k}^2}} \quad (40)$$

where

$$\gamma_{p,k} = \frac{4G_{s,p,k}\sqrt{R_1 R_2}}{(1 - \sqrt{R_1 R_2}G_{s,p,k})^2} \quad (41)$$

where the single-pass gain at energy $\hbar\omega_k$ and polarization p is given by

$$G_{s,p,k} = \exp\left[\int_0^L g_p(\hbar\omega_k, n)\,dz\right]. \quad (42)$$

If the facet reflectivities are equal to zero then $K_{p,k} = 1$.

V. STEADY-STATE NUMERICAL ALGORITHM

The SOA model equations cannot be solved analytically, so a numerical solution is required. In the model the SOA is split into N_t sections for each taper and N_c sections for the central region. A typical spatial step is shown in Fig. 5. The total number of sections is $N_z = 2N_t + N_c$. In the subsequent numerical algorithms we use $N_t = 3, N_c = 25$ and $N_s = 40$. Integrals with respect to k and θ use trapezoidal numerical integration with 400 and 12 points, respectively, and the ∞ limit for k is taken to be equal to 2×10^9 m^{-1}. The signal fields and ASE photon rates are estimated at the section interfaces. A flowchart of the algorithm used is shown in Fig. 6. The algorithm adjusts the carrier density in each section such that Q_i (the RHS of the carrier density rate equation) approaches zero (i.e., $dn/dt = 0$ for the
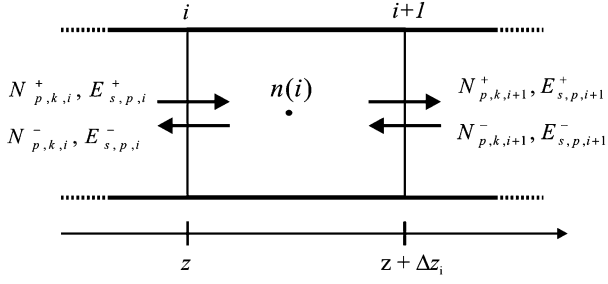
Fig. 5. The ith spatial section of the SOA showing the forward and backward traveling signal fields and noise photon rates. The carrier density is determined at the center of each section.
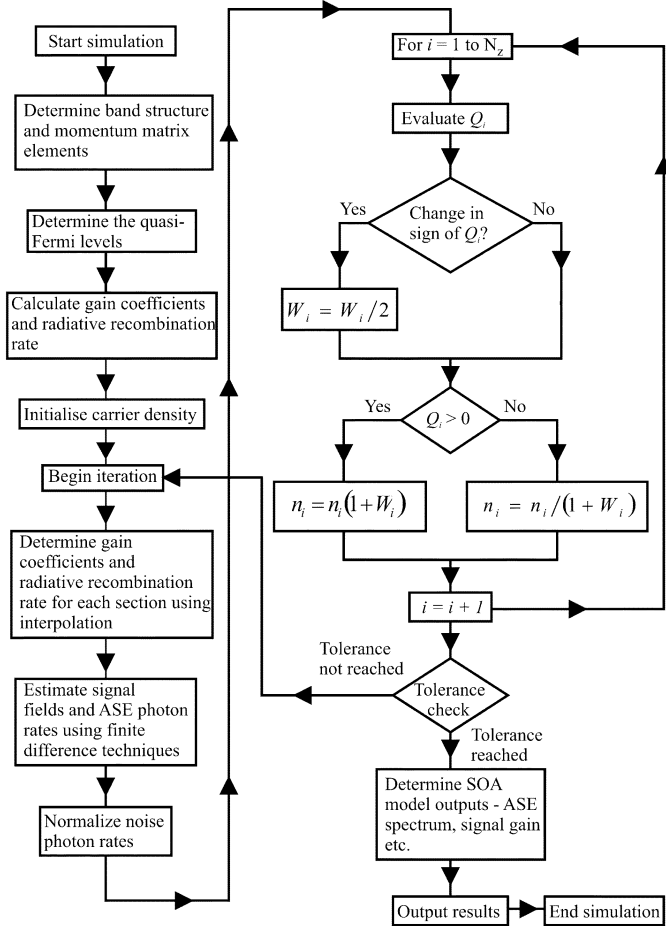

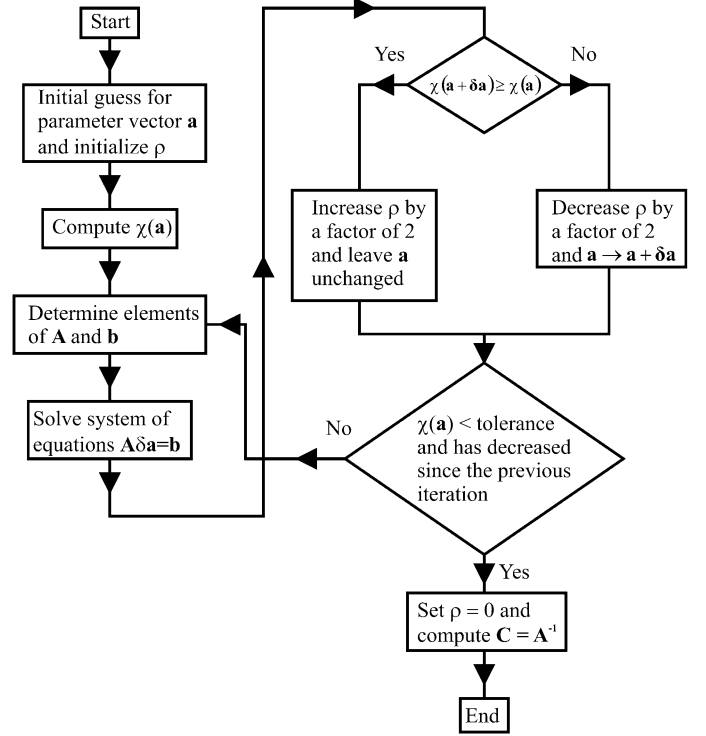Fig. 6. Flowchart of the steady-state algorithm.

Fig. 7. Flowchart of the SOA parameter extraction algorithm.

once for each run of the algorithm. The signal and ASE photon rates are initialized to zero and the carrier density throughout the SOA is initialized to some reasonable value (e.g., 3×10^{24} m^{-3}). The iteration now begins. First the gain coefficients for each section are determined using interpolation. The forward and backward propagating signal fields are determined from the finite difference solution to (26) given by

$$E_{s,p,i+1}^+ = E_{s,p,1}^+ \exp\left\{ \sum_{l=1}^{i} \left[\frac{1}{2} g_{p,l}\left(h\omega_s, n\right) - j\beta_{p,l} \right] \Delta z_i \right\}$$
$$i = 1, \ldots, N_z$$
$$E_{s,p,i}^- = E_{s,p,N_z+1}^- \exp\left\{ \sum_{l=i}^{Nz} \left[\frac{1}{2} g_{p,l}\left(h\omega_s, n\right) - j\beta_{p,l} \right] \Delta z_i \right\}$$
$$i = N_z, \ldots, 1 \quad (43)$$

subject to the boundary conditions (28). Δz_i is the spatial step of the ith section. The ASE photon rates are determined using the finite difference solutions to (31) given by

$$N_{p,k,i+1}^+ = N_{p,k,i}^+ \exp[g_{p,i-1}(h\omega_k, n)\Delta z_{i-1}]$$
$$+ R_{\mathrm{sp},p,i-1}(\hbar\omega_k, n)$$
$$\times \frac{\{\exp[g_{p,i-1}(h\omega_k, n)\Delta z_{i-1}] - 1\}}{g_{p,i-1}(h\omega_k, n)}$$
$$i = 2, \ldots, N_z + 1$$
$$N_{p,k,i}^- = N_{p,k,i+1}^- \exp[g_{p,i}(h\omega_k, n)\Delta z_i]$$
$$+ R_{\mathrm{sp},p,i}(\hbar\omega_k, n)$$
$$\times \frac{\{\exp[g_{p,i}(h\omega_k, n)\Delta z_i] - 1\}}{g_{p,i}(h\omega_k, n)}$$
$$i = N_z, \ldots, 1 \quad (44)$$

steady-state solution) for all sections. In evaluating Q_i for the ith section, the signal and noise photon rates used are given by the mean value of those quantities at the section boundaries. The first step in the algorithm is to determine the active region material band structure and matrix elements. Next the quasi-Fermi levels are determined from (14) and (15) using the numerical bisection method for the range of carrier densities likely to be found in the SOA as shown in Fig. 2. The polarization dependent material gain coefficients and radiative recombination rate are then determined for the same range of carrier density. This calculation is the most time consuming but only has to be done
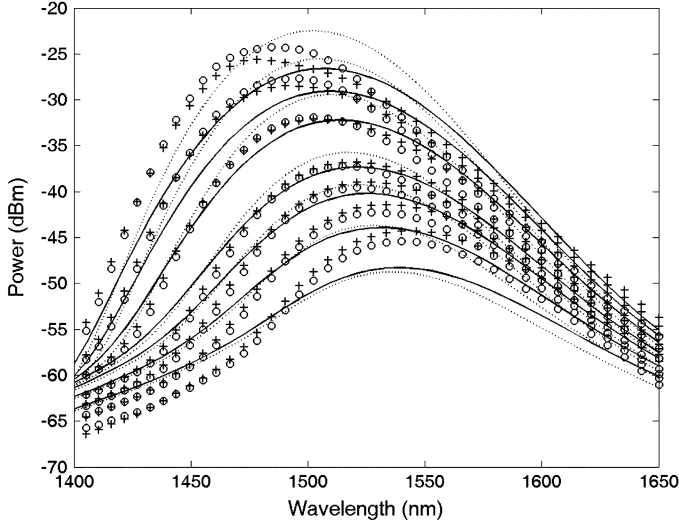
Fig. 8. Experimental and predicted SOA output ASE spectrum using the extracted model parameters. The bias currents are 40, 50, 60, 70, 100, 140, and 200 mA. The resolution bandwidth is 0.07 nm. The experimental ASE spectra gain ripple has been averaged out. "∘" and "+": experimental TM and TE spectra; solid line and dotted line: simulated ASE TM and TE spectra.

Fig. 10. Experimental and simulated fiber-to-fiber gain versus input power ("∘" and "+" experimental TM and TE polarization; solid and dotted lines—simulated TM and TE). The lowest, middle and higher set of curves/points correspond to signal wavelengths of 1563, 1550, and 1528 nm, respectively. The bias current is 200 mA.
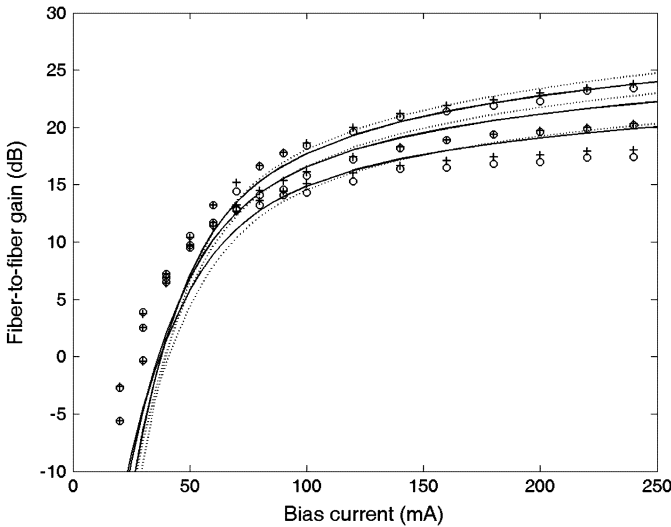

Fig. 9. Experimental and simulated fiber-to-fiber gain versus bias current (solid and dotted lines—TM and TE, "∘" and "+" experimental TM and TE). The input signal power is -14 dBm. The lowest, middle and highest set of curves/points correspond to signal wavelengths of 1563, 1550, and 1528 nm, respectively.

Fig. 11. Simulated carrier density spatial distributions for TM polarized signal input powers of -40 dBm (solid line), -10 dBm (dashed line) and 0 dBm (dotted line). The bias current and signal wavelength are 200 mA and 1550 nm, respectively.

subject to the boundary conditions (32). $N_{p,k,i}^{+}$ and $N_{p,k,i}^{-}$ are then multiplied by the normalization factor (40) and Q_i is calculated for each section. If Q_i is positive, then the estimated carrier density is too low, in which case the new value of carrier density for the section is the old value increased by a factor $1 + W_i$. W_i is a weighting factor whose absolute value is < 1. An initial value for W_i of 0.1 was found to give good convergence. If Q_i is negative, then the carrier density is too high, in which case the new value of carrier density for the section is the old value decreased by $1 + W_i$. If the sign of Q_i differs from the previous iteration, W_i is halved. This process enables convergence towards the correct value of carrier density throughout
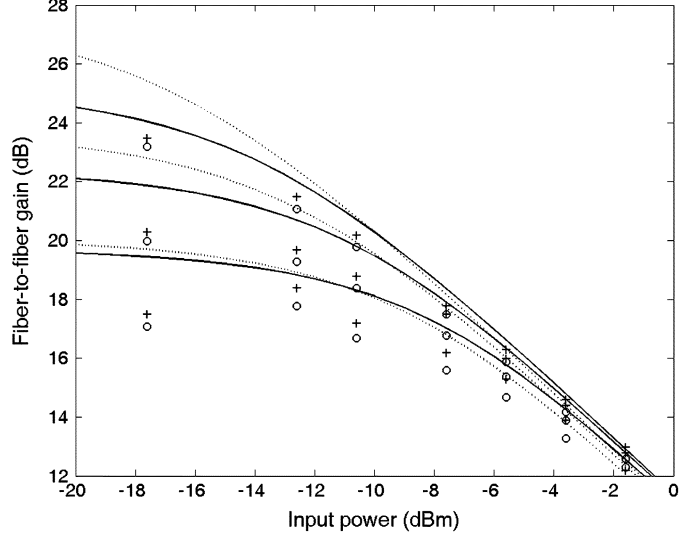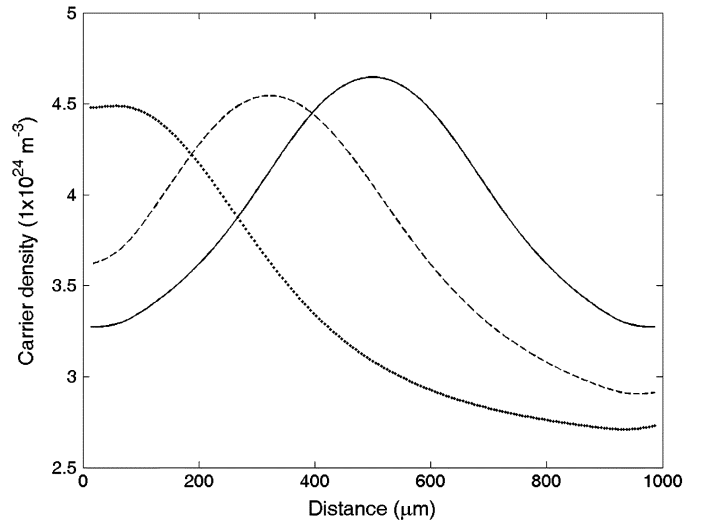
the SOA. The iteration continues until the absolute percentage change in the signal and ASE photon rates in the SOA between successive iterations is less than a desired tolerance (in this case 0.1%). When convergence has been achieved, relevant outputs such as the output ASE power spectral density (computed using the method described in [2]), signal gain and noise figure are calculated. In the case where $R_1 = R_2 = 0$, the output signal power is given by

$$P_{\text{out}} = \eta_{\text{out}} |E_{s,p,N_z+1}^{+}|^2 \hbar\omega_s \qquad (45)$$

where η_{out} is the output coupling loss. The output ASE noise power at energy $\hbar\omega$ and polarisation p in a resolution bandwidth
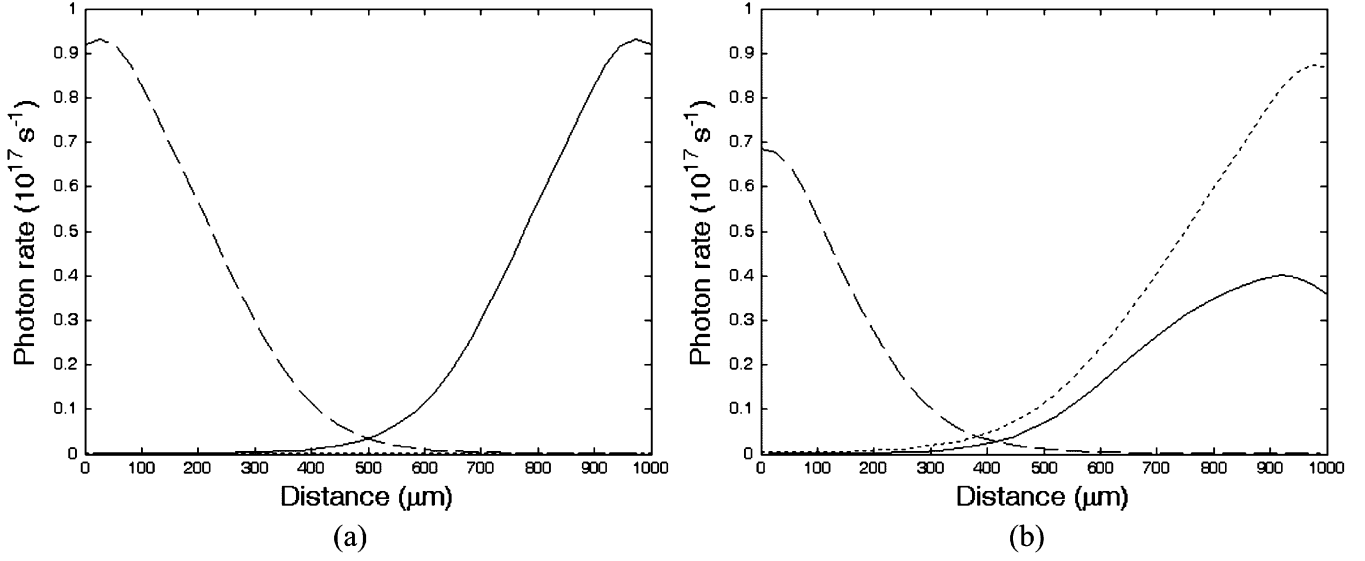
Fig. 12. ASE and signal spatial distributions for input TM signal powers (a) −40 dBm and (b) −12 dBm, with no input TE signal. Total forward propagating ASE (TE and TM)—solid line; Total backward propagating ASE (TE and TM)—dashed line and total forward propagating signal (dotted line). The bias current and signal wavelength are 200 mA and 1550 nm, respectively.

$\Delta\lambda_{\mathrm{res}}$ (as would be measured on an optical spectrum analyzer) is given by

$$P_{\mathrm{ASE},p}(\hbar\omega_k) = \eta_{\mathrm{out}} N^{-}_{p,k,Nz+1}(\hbar\omega_k)^3 \Delta\lambda_{\mathrm{res}}/hc. \quad (46)$$

VI. PARAMETER EXTRACTION

Because of the complexity of the model, which must apply over a broad wavelength range, it is necessary to determine the values of some of the material parameters used in the model. It is assumed that all of the model parameters are known with reasonable accuracy except for the actual values of y, C_{aug}, ε, and τ_r. The value of this parameter set for a given SOA is determined by using a parameter extraction algorithm that uses experimental polarization resolved ASE spectrum measurements at different bias currents and the steady-state algorithm described in Section V. The parameter extraction algorithm is based on the Levenberg–Marquardt method [14], [15], which is used to determine the SOA parameters that minimize the merit factor, which we define as the root-mean-square (r.m.s.) function

$$\chi = \frac{1}{2N_{\mathrm{exp}t}} \sum_{l=1}^{N_{\mathrm{exp}t}} \frac{1}{2} \sum_{p=\mathrm{TE,TM}}$$
$$\times \sqrt{\frac{1}{N_s} \sum_{k=1}^{N_s} |P_{\mathrm{ASE},p,l}(\hbar\omega_k) - P_{\mathrm{exp}t,p,l}(\hbar\omega_k)|^2} \quad (47)$$

where $P_{\mathrm{exp}t,p}$ is the experimental polarization resolved SOA output ASE spectrum. $P_{\mathrm{ASE},p}$ and $P_{\mathrm{exp}t,p}$ are in dBm. $N_{\mathrm{exp}t}$ is the number of experimental pairs of polarization resolved ASE spectra (at different bias currents). A flowchart of the parameter extraction algorithm is shown in Fig. 7. The set of unknown parameters (or for which a more accurate estimate is required) are combined in a parameter vector $\mathbf{a}$. The first step in the parameter extraction algorithm is to start with a reasonable guess for $\mathbf{a}$ and then compute $\chi(\mathbf{a})$. We then initialise a numerical parameter ρ

qual to a small value (e.g., 1). We then solve the linear equation set

$$\mathbf{A}\delta\mathbf{a} = \mathbf{b} \quad (48)$$

for $\delta\mathbf{a}$ the potential adjustment to $\mathbf{a}$, where the 4×4 matrix $\mathbf{A}$ has elements

$$A'_{qq} = A_{qq}(1 - \rho)$$
$$A'_{qr} = A_{qr}, \quad q \neq r, \qquad q, r = 1, \dots, 4 \quad (49)$$

with

$$A_{qr} = \sum_{l=1}^{N_{\mathrm{exp}t}} \sum_{p=\mathrm{TE,TM}} \sum_{k=1}^{N_s} \frac{\partial P_{\mathrm{ASE},p,l}(\hbar\omega_k)}{\partial a_q} \frac{\partial P_{\mathrm{ASE},p,l}(\hbar\omega_k)}{\partial a_r}. \quad (50)$$

The vector $\mathbf{b}$ has elements

$$b_q = \sum_{l=1}^{N_{\mathrm{exp}t}} \sum_{p=\mathrm{TE,TM}} \sum_{k=1}^{N_s} [P_{\mathrm{ASE},p,l}(\hbar\omega_k) - P_{\mathrm{exp}t,p,l}(\hbar\omega_k)]$$
$$\times \frac{\partial P_{\mathrm{ASE},p,l}(\hbar\omega_k)}{\partial a_q}. \quad (51)$$

Next $\chi(\mathbf{a} + \delta\mathbf{a})$ is calculated. If $\chi(\mathbf{a} + \delta\mathbf{a}) \geq \chi(\mathbf{a})$ then ρ is increased by a factor of 2 and $\mathbf{a}$ is left unchanged otherwise $\mathbf{a}$ is updated to $\mathbf{a} + \delta\mathbf{a}$ and ρ is decreased by a factor of 2. This process is continued until $\chi(\mathbf{a})$ is less than a desired tolerance and has decreased since the previous iteration. After convergence has been achieved ρ is set equal to 0 and the matrix $\mathbf{C} = \mathbf{A}^{-1}$ is computed, which is the estimated covariance matrix of the standard errors in the fitted parameters. The diagonal elements of $\mathbf{C}$ are the variances of the elements of $\mathbf{a}$.

To determine the parameters of the SOA polarisation resolved spectra at bias currents of 40, 50, 60, 70, 100, 140, and 200 mA were used with a wavelength range from 1400–1650 nm. The SOA temperature was 300 K. The input signal power was zero. It
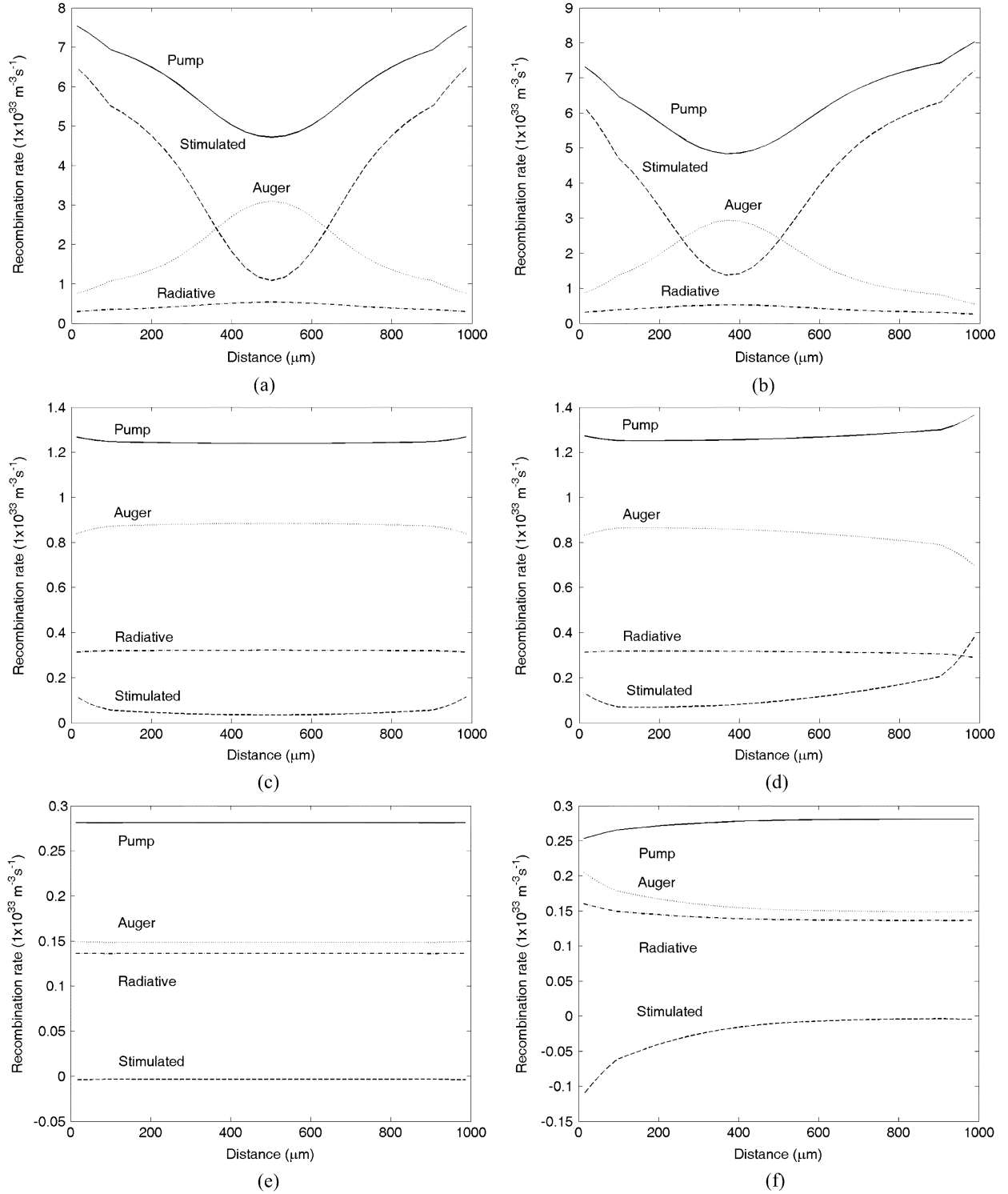
Fig. 13. Pump and recombination terms on the RHS of (36). The input signal wavelength is 1550 nm and is TM polarized. (a) Bias current $= 200$ mA and input signal power $= -40$ dBm; (b) Bias current $= 200$ mA and input signal power $= -12$ dBm; (c) Bias current $= 50$ mA and input signal power $= -40$ dBm; (d) Bias current $= 50$ mA and input signal power $= -12$ dBm. (e) Bias current $= 10$ mA and input signal power $= -40$ dBm. (f) Bias current $= 10$ mA and input signal power $= 0$ dBm.

is assumed that the facet reflectivities are equal to zero. The parameters determined were $y = 0.816, \tau_r = 22.4$ fs, $\varepsilon = 0.15\%$ and $C_{\mathrm{aug}} = 2.8 \times 10^{-41}$ m^{6}s^{-1} with standard deviations (as a percentage of the mean values) of 0.7%, 0.03%, 1%, and 1%, respectively, which is a measure of the uniqueness of the extracted parameters. The algorithm converged to a limiting value

of $\chi(\mathbf{a}) = 2.3$ dB. The relatively low value of τ_r is due to the relatively wide gain bandwidth of the SOA. The extracted value of strain is lower than the nominal value, which is attributed to strain relaxation. The extracted value of C_{aug} is similar to that of $-B_1$, which indicates that there is no significant cubic term in the total recombination rate of (39). However, the dif-

ference is still significant over the range of carrier densities typically present in the SOA. The extracted value of C_{aug} is not directly dependent on the value of B_1 in the cubic polynomial fit to B_{rad}, but depends on the total radiative recombination rate and the other terms on the RHS of (36). A comparison between the experimental and predicted ASE spectra (using the extracted parameters) is shown in Fig. 8.

VII. PREDICTION OF STEADY-STATE SIGNAL AMPLIFICATION CHARACTERISTICS

As shown in Fig. 8, there is a good wide-band agreement between the simulated and experimental ASE spectra for the set of model parameters used. The applicability of the model parameters to predicting the wide-band steady-state signal gain characteristics of the SOA is shown in Figs. 9 and 10, which show experimental and simulated SOA fiber-to-fiber polarization resolved signal gain versus bias current and SOA gain versus input signal power characteristics at three different wavelengths, within the usual operating wavelength range of the SOA. As shown in Figs. 9 and 10, there is good agreement between the model predictions and experiment. The model can be used to determine the carrier density and photon density spatial distributions in the SOA. In Figs. 11 and 12, typical spatial distributions are shown for the SOA at a bias current of 200 mA with low- and high-input signal powers. As the input signal power increases the carrier density distribution becomes more asymmetrical due to the increasing dominance of the forward propagating signal. The associated mechanisms responsible for the carrier density depletion are shown in Fig. 13. At a high bias current (200 mA) and both for low and high input signal power the dominant recombination mechanisms, as shown in Fig. 13(a) and (b), are stimulated emission and Auger recombination with the radiative recombination having a relatively small contribution. In the case of a moderate bias current (50 mA) and low input signal power the dominant recombination mechanisms are Auger and radiative recombination as shown in Fig. 13(c). In the case of the moderate bias current (50 mA) and high input signal power all of the recombination mechanisms are important as shown in Fig. 13(d). In the case of the low bias current (10 mA), where the SOA is gain is <0 dB, and low input signal power, radiative and Auger recombination are almost equally important as shown in Fig. 13(e). Stimulated recombination in this case is almost negligible. In the case of the low bias current (10 mA) and high input signal power, radiative and Auger recombination are almost equally important as shown in Fig. 13(e). The stimulated emission term in this case is negative and actually generates carriers, via net stimulated absorption. A similar situation exists in the case of low bias and high input power as shown in Fig. 13(f). Fig 13 also shows the effect of pump blocking, which is particularly apparent at high bias currents due to the high injected carrier density. The relatively abrupt changes in the spatial distributions of Figs. 11–13 at the 100-μm and 900-μm positions are due to the change in the optical confinement factors at those points, where the linear tapers begin. In Fig. 12, the total ASE and signal photon rate decreases slightly in the output taper region. The corresponding recombination term in the carrier density rate equation as shown in Fig. 13(a) and (b) increases in the taper region. This apparent contradiction is because the ratio of the confinement factors to the taper width increases as the taper

width decreases. It is often of interest in SOA design to determine the influence of the active region thickness on the device characteristics such as saturation output power. This would require detailed information on the dependence of the confinement factors on the active region thickness [5].

VIII. CONCLUSION

A wide-band steady-state model, including a parameter extraction algorithm, of a tensile-strained bulk InGaAsP semiconductor optical amplifier has been described. The model predictions show good agreement with experiment. The model can be used to investigate the effects of different material and geometrical parameters on SOA performance under operating conditions ranging from low and high bias currents and input signal powers and over a wide range of input signal wavelengths.

REFERENCES

[1] M. J. Connelly, *Semiconductor Optical Amplifiers*. Boston, MA: Springer-Verlag, 2002.
[2] ——, "Wide-band semiconductor optical amplifier steady-state numerical model," *IEEE J. Quantum Electron.*, vol. 37, no. 3, pp. 439–447, Mar. 2001.
[3] ——, "Wideband dynamic numerical model of a tapered buried ridge stripe semiconductor optical amplifier gate," in *Proc. IEE Circuits Devices Syst.*, 2002, vol. 149, pp. 173–178.
[4] G. P. Agrawal and N. K. Dutta, *Long Wavelength Semiconductor Lasers*. New York: Van Nostrand Reinhold, 1986.
[5] K. Morito, M. Ekawa, T. Watanabe, and Y. Kotaki, "High-output-power polarization-insensitive semiconductor optical amplifier," *J. Lightw. Technol.*, vol. 21, no. 1, pp. 176–181, Jan. 2003.
[6] T. Kakitsuka, Y. Shibata, M. Itoh, Y. Kadota, Y. Tohmori, and Y. Yoshikuni, "Influence of buried structure on polarization sensitivity in strained bulk semiconductor optical amplifiers," *IEEE J. Quantum Electron.*, vol. 38, no. 1, pp. 85–92, Jan. 2002.
[7] S. L. Chuang, *Physics of Optoelectronic Devices*. New York: Wiley, 1995.
[8] T. Suhara, *Semiconductor Laser Fundamentals*. New York: Marcel Dekker, 2004.
[9] G. Jones and E. P. O'Reilly, "Improved performance of long-wavelength strained bulk-like semiconductor lasers," *IEEE J. Quantum Electron.*, vol. 29, no. 5, pp. 1344–1345, May 1993.
[10] W. W. Chow and S. W. Koch, *Semiconductor Laser—Fundamentals*. New York: Springer-Verlag, 1999.
[11] J. P. Weber, "Optimization of the carrier-induced effective index change in InGaAsP waveguides-application to tunable Bragg filters," *IEEE J. Quantum Electron.*, vol. 30, no. 8, pp. 1801–1816, Aug. 1994.
[12] F. Jahnke and S. W. Koch, "Theory of carrier heating through injection pumping and lasing in semiconductor microcavity lasers," *Opt. Lett.*, vol. 18, no. 17, pp. 1438–1440, 1993.
[13] M. J. Connelly, "Corrections to "Wideband semiconductor optical amplifier steady-state numerical model"," *IEEE J. Quantum Electron.*, vol. 37, no. 8, p. 1103, Aug. 2001.
[14] W. H. Press, B. P. Flannery, S. A. Teukolsky, and W. T. Vetterling, *Numerical Recipes in Pascal*. Cambridge, U.K.: Cambridge Univ. Press, 1994.
[15] M. J. Connelly, "Semiconductor optical amplifier parameter extraction using a wide-band steady-state numerical model and the Levenberg–Marquardt method," in *Proc. 4th IEEE Int. Conf. Numer. Simul. Optoelectron. Dev.*, 2004, pp. 38–39.

Michael J. Connelly (S'89–M'92) was born in Limerick, Ireland, in 1965. He received the B.E. and Ph.D. degrees in electronic engineering from the National University of Ireland, Dublin, Ireland, in 1987 and 1992, respectively.

He is a Senior Lecturer in Electronic Engineering and Director of the Optical Communications Research Group at the University of Limerick. The current research interests of the group include all-optical signal processing using SOAs, optical coherence tomography, and laser vibrometry.